Journal of Alloys and Compounds 1037 (2025) 182416

Contents lists available at ScienceDirect

Journal of Alloys and Compounds

journal homepage: www.elsevier.com/locate/jalcom

Nano-blade structured hematite/magnetite heterojunction with ZnO cocatalyst and plasmon Au adornment for improvement in solar water splitting

Jiaheng Gao, Maojun Zheng *, Hao Yuan, Ying Yang, Hao Chen, Yunlong Fan, Wenzhong Shen

Ministry of Education Key Laboratory of Artificial Structures and Quantum Control, School of Physics and Astronomy, Shanghai Jiao Tong University, Shanghai 200240, PR China

ARTICLE INFO

Keywords:
Hematite photoanodes
Solar water splitting
ZnO cocatalyst
Au nanoparticles
Heterojunction
Localized surface plasmon resonance

ABSTRACT

In this study, ZnO cocatalyst and plasmonic Au nanoparticles were introduced to nano-blade structured α-Fe_2O_3/Fe_3O_4 heterojunction photoanodes, fabricated via direct oxidation annealing of high-purity iron foil, for enhanced photoelectrochemical (PEC) water splitting. The optimal sample annealed at 300 °C exhibited a photocurrent density of 0.580 mA cm^{-2} (1.6 V vs. RHE), attributed to its slender nano-blade morphology and internal heterojunction. Subsequent surface modifications using zinc acetate spin-coating and Au nanoparticle deposition increased the photocurrent density to 1.006 mA cm^{-2}, marking a 73.4 % enhancement over pristine hematite. ZnO facilitated favorable band alignment, while Au nanoparticles induced localized surface plasmon resonance (LSPR) and enabled hot-electron injection. Both modifications also increased surface oxygen vacancy concentration, collectively improving charge separation and transfer. Moreover, the photoanode demonstrated excellent stability over 20 h of continuous operation, highlighting its potential for practical PEC applications.

1. Introduction

With the fast-paced advancements in science and technology, the demand for energy is rising significantly. Fossil fuels remain the dominant energy source but pose significant harms. According to the 2023 report by the IEA (International Energy Agency), the total global energy consumption in 2022 was approximately 4.42×10^{20} J, with fossil fuels accounting for about 76 %. The global energy supply in 2022 was 6.32×10^{20} J, with fossil fuels accounting for approximately 80 % [1]. The reliance on fossil fuels may cause economic and even social instability due to fluctuating prices and resource scarcity. Additionally, combusting fossil fuels emits greenhouse gases, exacerbating global warming and climate change, and the extraction of fossil fuels generate air and water pollutants that may lead to respiratory and cardiovascular diseases as well as environmental degradation. Transitioning to renewable energy sources is imperative to mitigate these severe impacts. Renewable energy sources include solar, wind, hydroelectric, geothermal, and biomass energy. Among these, the utilization and development of solar energy have become the most advanced. Modern solar energy technology can be categorized into three main areas. The first is solar collectors that convert solar energy into thermal energy. The second is photovoltaic cell technology, which focuses on transforming solar energy into electrical energy. The third technology converts solar energy into chemical energy, known as PEC cell technology. Specifically, PEC cell for water splitting generates hydrogen, a promising clean fuel known owing to its high energy density, ranging from 120 to 142 MJ kg^{-1}. Research on PEC water splitting dates back to the pioneering work by Fujishima and Honda in 1972, where they employed single-crystal TiO_2 (rutile) anode along with Pt cathode, establishing a PEC water-splitting system under ultraviolet light irradiation [2]. This research provided groundbreaking evidence for the feasibility of utilizing semiconductor material electrodes in photocatalytic water splitting, thereby sparking significant interest and enthusiasm in the study of semiconductor materials for photoelectrode.

In recent years, semiconductor materials for PEC water splitting have primarily included metal oxides [3–5], sulfides [6–8], noble metal semiconductors [9,10], and non-metal semiconductors [11–13]. Among oxide semiconductors, hematite(α-Fe_2O_3) is considered a prominent

* Corresponding author.
E-mail address: mjzheng@sjtu.edu.cn (M. Zheng).

https://doi.org/10.1016/j.jallcom.2025.182416
Received 23 March 2025; Received in revised form 18 July 2025; Accepted 20 July 2025
Available online 21 July 2025
0925-8388/© 2025 Elsevier B.V. All rights are reserved, including those for text and data mining, AI training, and similar technologies.

candidate for PEC electrode materials. It is inexpensive, non-toxic, and readily available. Hematite is plentiful in nature, as iron is the fourth most prevalent element in the Earth's crust, making up roughly 6.3 % [14]. Additionally, α-Fe_2O_3 exhibits good chemical stability and resistance to photo-corrosion. Possessing a bandgap of 2.1–2.3 eV, α-Fe_2O_3 can harvest a broad range of the solar spectrum, reaching a maximum wavelength of 590 nm, theoretically enabling it to capture 38 % of solar light, including 33 % from visible light and 5 % from ultraviolet light [15]. However, α-Fe_2O_3 still has many pressing issues that need to be resolved, such as its low conductivity (10^{-14}–10^{-6} Ω^{-1} cm^{-1}) and short carrier lifetime (on the order of picoseconds), as well as its low mobility of minor carriers (holes), approximately 0.2 cm^2 V^{-1} s^{-1}, resulting in a short diffusion distance of 2–4 nm. Poor kinetics in water oxidation of α-Fe_2O_3 also limit its PEC efficiency [16–20]. Due to the limitations of α-Fe_2O_3, numerous modification attempts have been made. For instance, Dhandole et al. explored the enhancement of hematite photoanodes via co-doping with niobium (Nb) and zirconium (Zr) for PEC water splitting. Co-doped photoanodes demonstrated a significant 111 % increase in photocurrent density in comparison of undoped hematite photoanodes, which is attributed to Zr's enhancement of bulk charge transfer and Nb's suppression of surface charge recombination, collectively leading to efficient and stable water splitting performance [21]. Ahmed etc. managed to deposit a CeO_x overlayer on hematite. Their study demonstrated a substantial photocurrent increase, reaching up to three times that of pristine hematite. This improvement in the efficiency of hole injection, catalytic activity at the surface, and interfacial charge transport between the photoanode and electrolyte is attributed to the combined effort of Ce^{3+}/Ce^{4+} redox species and oxygen vacancies in the CeO_x overlayer [22]. Selvaraj Seenivasan et al. deposited an ultrathin $NiFeO_x$ layer on hematite through atomic layer deposition (ALD), optimizing its composition and thickness to improve PEC water splitting and pollutant degradation. Their research revealed a notable increase in photocurrent density, along with improved charge separation and transfer efficiency. This improvement can be ascribed to the surface state passivation and the establishment of a new charge transfer pathway, leading to better performance in solar water splitting and the organic pollutant degradation, such as tetracycline hydrochloride [23].

Although numerous studies have reported various modification strategies to enhance the PEC performance of α-Fe_2O_3 photoanodes, each strategy only addresses part of the intrinsic limitations of the material; therefore, multi-step modification approaches have been employed to construct composite photoelectrode systems. For instance, Subramanian et al. achieved an over 70 % photocurrent enhancement at 1.23 V vs. RHE on hematite photoanodes through Zr^{4+}/Al^{3+} co-doping and CoO_x surface treatment, which suppressed surface recombination, lowered charge-transfer resistance, and shifted the onset potential cathodically [24]. Kang et al. reported that introducing an ultrathin SiO_2 insulating under-layer beneath a Ti-doped hematite film effectively suppressed back electron recombination at the FTO/hematite interface, thereby facilitating interfacial charge transfer and yielding a 52 % photocurrent density enhancement at 1.6 V vs. RHE [25]. Herein, we employed a dual-modification strategy by introducing a ZnO cocatalyst and plasmonic Au nanoparticles onto a nano-blade structured α-Fe_2O_3/Fe_3O_4 heterojunction photoanode. The α-Fe_2O_3 films were fabricated on an Fe substrate via direct oxidation annealing of high-purity iron foil in air. We managed to develop nano-blade structured α-Fe_2O_3/Fe_3O_4 heterojunction when Fe foil was annealed at 300 °C. The sample exhibited the best PEC performance among samples prepared at different annealing temperatures, achieving an optimal photocurrent density of 0.580 mA cm^{-2} (1.6 V vs. RHE). A two-step modification method was employed subsequently. Firstly, previously prepared α-Fe_2O_3 samples (annealed at 300 °C) were treated with a zinc acetate ethanol solution using spin coating and then annealed to introduce ZnO to get α-Fe_2O_3/ZnO samples. Secondly, the α-Fe_2O_3/ZnO samples were immersed in a chloroauric acid solution to introduce and deposit Au nanoparticles for modification. After modification, the α-Fe_2O_3/ZnO/Au sample exhibits a photocurrent density of 1.006 mA cm^{-2} (1.6 V vs. RHE), representing a 73.4 % increase compared to pristine α-Fe_2O_3 sample.

2. Experimental method

2.1. Fabrication of α-Fe_2O_3 on Fe substrate

α-Fe_2O_3 samples were fabricated via oxidative annealing in air. High-purity iron foils (4 N, 99.99 %) were used as both raw material and substrate, purchased from Zhongkeyannuo Company. The iron foils were first cut into small sections of around 1 cm × 1 cm, then flattened and polished with 400-grit and 2000-grit sandpaper. This step aimed to eliminate the initial oxide layer and any surface contaminants from the iron foil. Secondly, the small pieces of iron foil were ultrasonically cleaned with acetone and anhydrous ethanol for 10 min each. This step was performed to remove oil stains from the iron foil surface. The foils were then rinsed 3–5 times with deionized water and dried with nitrogen gas. Subsequently, the cleaned iron foils were immersed in a 5 mM $HAuCl_4$ aqueous solution for 1 min. This process deposited a modest quantity of Au nanoparticles onto the iron foil surface, serving as a seed layer to provide active sites for surface oxidation and promoting the growth of nanostructures [26]. Finally, the iron foils were dried with nitrogen gas and then annealed in air with a muffle furnace (Yamato, FO 100). The annealing temperatures were chosen at 250 °C, 300 °C, 350 °C, 400 °C, 450 °C, and 500 °C. During oxidation annealing process, a temperature ramp of 10 °C min^{-1} was established. After reaching the target annealing temperature, it was maintained for 2 h and cooled to room temperature.

2.2. Fabrication of ZnO layer

The prepared α-Fe_2O_3 samples annealed at 300 °C (denoted as **300°C-2h**) were spin-coated and annealed to introduce a layer of ZnO to the sample surface. The samples were spin-coated with a 25 mM zinc acetate ethanol solution ((Sigma Aldrich, 99.9 %), 40 μL of zinc acetate ethanol solution was used for each spin-coating process. Spin-coating was conducted at 3000 r min^{-1} for 30 s and repeated twice, followed by natural drying and annealing. The annealing temperature was set to 400 °C (zinc acetate completely decomposes into zinc oxide at 370 °C). The heating rate was set to 10 °C min^{-1} , and it was maintained for 2 h at 400 °C, followed by cooling to room temperature. This step introduced a ZnO layer with an appropriate thickness onto the surface of the α-Fe_2O_3 sample, fabricating α-Fe_2O_3/ZnO samples (denoted as **300°C-2h-SC2-A1**).

2.3. Au nanoparticles decoration

The α-Fe_2O_3/ZnO samples were immersed in a 5 mM $HAuCl_4$ (Sigma Aldrich, 99.9 %) aqueous solution with the nanostructured surface facing downwards for 3 h, then rinsed with deionized water and dried with nitrogen gas for adornment with Au nanoparticles. A shorter immersion time may result in unsuccessful attachment of Au nanoparticles, while an excessively long immersion time could lead to significant damage to the hematite nanostructure. The final product was α-Fe_2O_3/ZnO/Au samples (denoted as **300°C-2h-SC2-A1-Au3h**).

2.4. Photoelectrochemical characterization

The backsides of the prepared photoanodes were polished to remove the oxide layer. SPI conductive silver paste (purchased from Zhongjingkeyi) was used to connect the samples with copper wires. The backside of the electrode was completely encapsulated with epoxy resin to prevent contact with the electrolyte, which could cause leakage and affect the test results, thus forming the photoelectrode.

PEC characterization was carried out using a three-electrode system,

with the prepared α-Fe_2O_3-based photoanode as the working electrode, a Pt mesh as the counter electrode, and an Ag/AgCl (saturated KCl solution) electrode as the reference electrode. The conversion equation between the reversible hydrogen electrode (RHE) and the reference electrode (Ref) is as follows:

$$E_{RHE} = E_{Ag/AgCl} + 0.059pH + E^0_{Ag/AgCl} \quad (1)$$

$E_{Ag/AgCl}$ represents the applied external bias voltage (relative to the reference electrode), and $E^0_{Ag/AgCl}$ is 0.1976 V at room temperature. The electrolyte was 1 M NaOH (pH = 13.6). A xenon light source (SOLARDGE 700 simulator) served as illumination for tests involving photoresponse, with the power density set to 100 mW cm^{-2} on the photoanode surface. An electrochemical workstation (VersaSTAT 4, Princeton Applied Research) was used as the power supply to provide the required external bias voltage for the tests and to collect data for further analysis. The photocurrent density is used to evaluate the PEC efficiency of semiconductor photoelectrodes.

The Mott-Schottky test was performed in darkness, with frequency set to 1000 Hz and a scan rate of 10 mV s^{-1}. The external bias voltage applied ranged from −0.8 to 0.8 V vs. Ref (equivalent to 0.2–1.8 V vs. RHE). Data points were collected every 40 mV.

The electrochemical impedance spectroscopy (EIS) test was conducted at an external bias voltage of 0.6 V vs. Ag/AgCl (equivalent to 1.6 V vs. RHE). The scanning frequency was set from 10^5 to 0.1 Hz, with a perturbation signal of 20 mV sine wave. This test was conducted in a dark environment as well.

2.5. Other characterizations of α-Fe_2O_3 based photoanodes

The sample morphology was examined via general-purpose field emission scanning electron microscope (FESEM, Sigma 300). High-resolution transmission electron microscopy (HRTEM) analysis was carried out using a 200 kV field-emission transmission electron microscope (Talos F200X G2). The TEM samples were prepared using a focused ion beam scanning electron microscope (FIB-SEM) system (Helios 5 CX). The composition of the samples was analyzed using XRD, Raman and XPS tests. The XRD test was performed with an X-ray diffractometer (Haoyuan DX-2700BH), with a tube voltage of 40 kV and a tube current of 30 mV, while the scan angle was set from 20 ° to 70 ° with a step width of 0.02 °. The Raman test was performed via a confocal micro-Raman spectrometer (Renishaw inVia Qontor) at room temperature, with a laser wavelength of 532 nm, a maximum output of 25 mW, and a 100x objective lens. The UV–vis diffuse reflectance spectroscopy (UV–vis DRS) was conducted to evaluate the light absorption properties of the synthesized samples. The measurements were performed using a UV-Vis-NIR spectrophotometer (Lambda 950) in reflectance mode (R %). The spectral range was set from 400 to 1000 nm, with a data interval of 1 nm. Photoluminescence (PL) and time-resolved fluorescence (TRF) measurements were performed using a steady-state/transient fluorescence spectrometer (FLS1000) to investigate the charge carrier separation efficiency of the samples. An excitation wavelength of 410 nm was selected for the measurements. An X-ray photoelectron spectrometer (AXIS UltraDLD) was used for XPS tests, with Al Kα as the X-ray source, aiming to analyze the valence state and composition of the sample surface structure.

3. Results and discussion

Overall fabrication process is shown in Fig. 1. We employed structural, morphological, PEC, as well as spectroscopic characterizations on the α-Fe_2O_3 samples annealed at different temperatures, the α-Fe_2O_3/ZnO sample and the α-Fe_2O_3/ZnO/Au prepared via modification treatments.

3.1. Structural characterization

To verify the composition of the samples prepared, XRD, Raman, XPS and EDX tests were conducted. From the XRD patterns of samples annealed at different temperatures (Fig. 2a), it can be observed that the main components of all the prepared samples are α-Fe_2O_3 and Fe_3O_4, which correspond with the standard PDF cards (Hematite: PDF#72–0603, Magnetite: PDF#26–1136). At 250 °C, The Fe_3O_4 peaks dominate the XRD patterns, with only weak α-Fe_2O_3 peaks. As the annealing temperature increases, the α-Fe_2O_3 peaks gradually become dominant, while the Fe_3O_4 peak responses weaken progressively. When the annealing temperature reaches 450 °C, Fe_3O_4 peaks almost

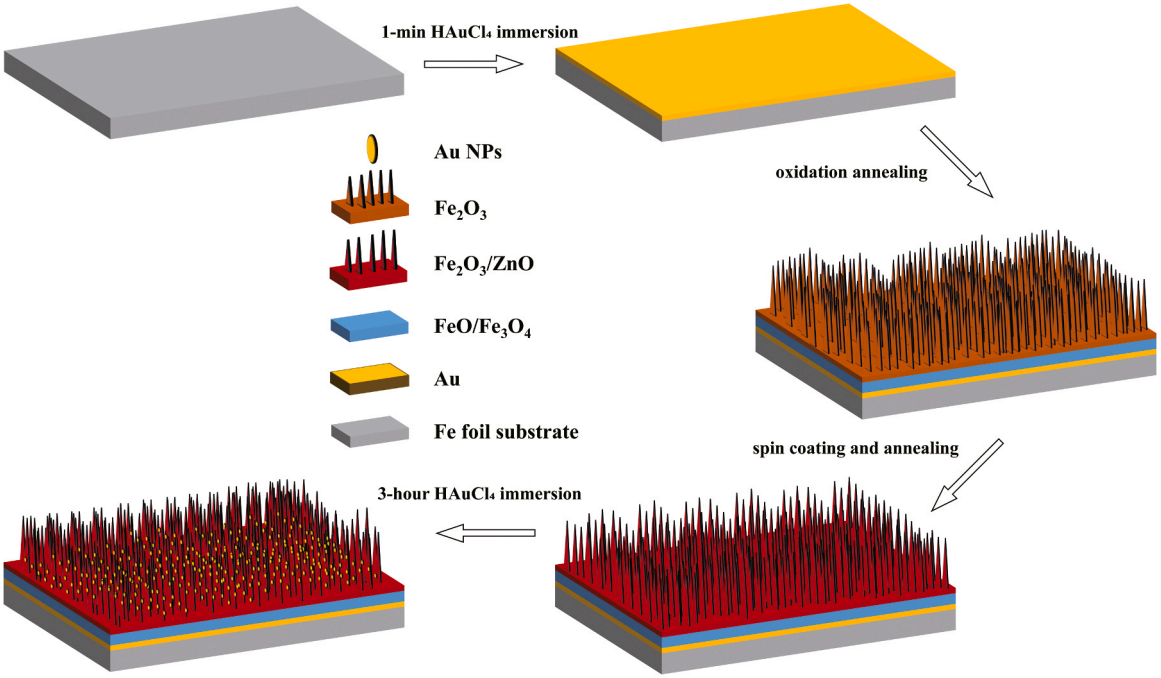

Fig. 1. Fabrication of α-Fe_2O_3/ZnO/Au photoanode.

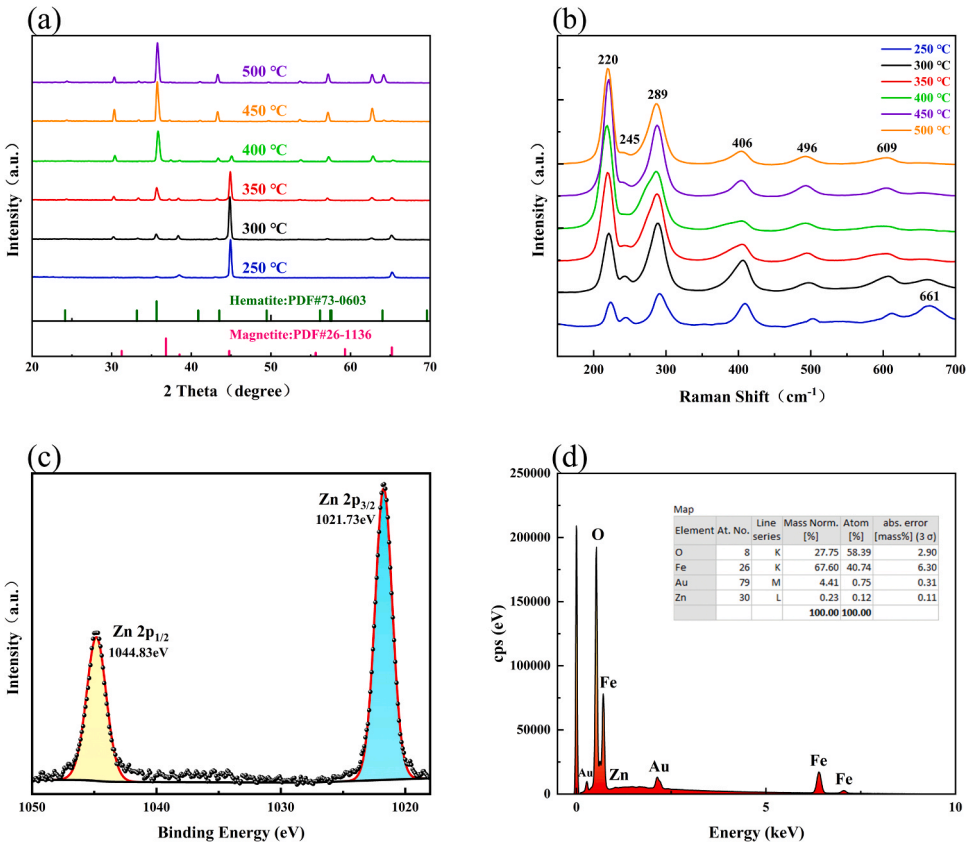

Fig. 2. (a) XRD spectra; (b) Raman spectra of α-Fe_2O_3 samples fabricated at different annealing temperatures 250 °C, 300 °C, 350 °C, 400 °C, 450 °C, 500 °C. (c) XPS spectra of α-Fe_2O_3/ZnO sample (Zn 2p scan). (d) Overall EDX spectrum of α-Fe_2O_3/ZnO/Au sample.

completely disappeared.

From the Raman spectra (Fig. 2b), it can be observed that all samples exhibit the characteristic peaks of α-Fe_2O_3 (which belongs to the D^6_{3d} space group). Specifically, the characteristic peaks at 220 and 496 cm^{-1} correspond to the A_{1g} mode, while the peaks at 245, 289, 406, and 609 cm^{-1} belong to the E_g mode. For samples annealed at 250 °C and 300 °C, a characteristic peak at 661 cm^{-1} is also observed, which is associated with Fe_3O_4 [27]. Combined with the results of XRD and Raman tests, we can conclude that when annealing, the iron foil surface first developed a layer of Fe_2O_3 due to complete oxidation. However, the subsequent reaction lacks sufficient motivation due to low oxygen partial pressure, leading to incomplete oxidation at the Fe_2O_3/Fe interface, forming a layer of Fe_3O_4. Likewise, we obtained a layered structure of Fe_2O_3/Fe_3O_4/FeO/Fe ultimately [28], and the content of FeO is negligible. As the annealing temperature increases, the oxidation reaction becomes more vigorous, with Fe_2O_3 increasingly becoming more dominant due to more complete oxidation, while the proportion of Fe_3O_4 decreases.

To confirm the successful introduction of ZnO, XPS characterization was performed on the **300°C-2h-SC2-A1** sample, where the Zn $2p_{1/2}$ and Zn $2p_{3/2}$ peaks were observed (Fig. 2c), consistent with the characteristic peaks of zinc oxide[29]. Fig. 2d presents the overall EDX spectrum of the sample **300°C-2h-SC2-A1-Au3h**, showing that Au nanoparticles were successfully introduced onto the sample **300°C-2h-SC2-A1** as surface modification.

3.2. Morphological characterization

α-Fe_2O_3 samples prepared under different annealing temperatures showed significant differences in surface morphology. Additionally, we prepared samples annealed at 200 °C and 550 °C as controls. When annealed at 200 °C, the sample surface almost remained similar to the pre-reaction state, retaining a shiny silver-gray color, while annealed at 550 °C, the surface exhibited peeling and defects due to the high temperature. Furthermore, no obvious photo response was detected for the samples annealed at 200 °C, and the photocurrent density was lower than 0.1 mA cm^{-2} for the samples annealed at 550 °C. Therefore, we selected annealing temperatures of 250 °C, 300 °C, 350 °C, 400 °C, 450 °C, and 500 °C to investigate the performance of α-Fe_2O_3 samples at different annealing temperatures.

Fig. 3a–f show the SEM images of the surface morphology of samples prepared with a 2-hour annealing time at annealing temperatures of 250 °C, 300 °C, 350 °C, 400 °C, 450 °C, and 500 °C, respectively. At an annealing temperature of 250 °C, the sample developed thin and loosely packed "nanowire" structures resembling wild grass on the surface, with the width of the "nanowires" generally less than 50 nm. At 300 °C, the sample surface exhibited uniform, slender blade-like structures that were quite dense, with widths ranging from approximately 80 to 120 nm. At 350 °C, the sample surface continued to show uniform and dense "nano-blade" structures, but wider, with widths of about 150–300 nm. At 400 °C, the sample surface displayed leaf-like structures, the width of the "nano-leaves" ranged approximately 250–500 nm. At 450 °C, the surface presented broader, shorter flower-like "nano-petals", with widths ranging from about 300–550 nm. At 500 °C, the petal-like structures became even broader and shorter, with a decrease in density and uniformity, and the widths varied between 300 and 900 nm. In some areas, the sample surface revealed clump-like structures resembling "stamens".

After undergoing the spin-coating and annealing treatment, the prepared α-Fe_2O_3/ZnO sample surface became rougher and took on a deeper brown color, and then shifted to yellow-brown after subsequent treatment of being immersed in a chloroauric acid solution. Fig. 3g–l present the SEM and EDX images of the sample **300°C-2h-SC2-A1-Au3h**. As shown in Fig. 3g, after the spin-coating and annealing

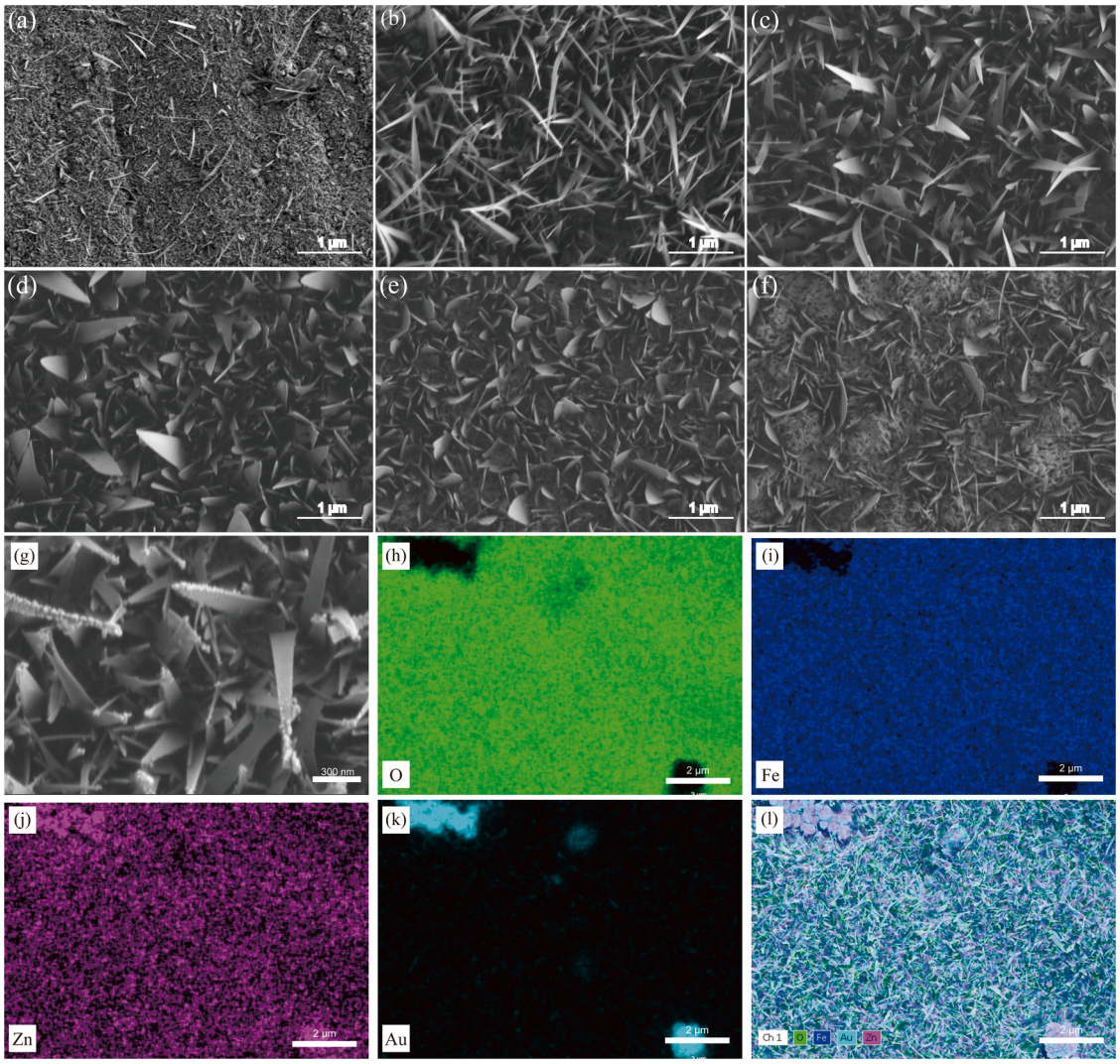

Fig. 3. SEM images of the samples fabricated at different annealing temperatures, (a) 250 °C; (b) 300 °C; (c) 350 °C; (d) 400 °C; (e) 450 °C; (f) 500 °C. SEM image and EDX mapping of α-Fe_2O_3/ZnO/Au sample, (g) SEM image, (h) O (i) Fe (j) Zn (k) Au (l) 4-element overall EDX images. Magnification is 20 k.

treatment, the sample surface still maintained a uniform and dense elongated nano-blade structure. Additionally, small particles can be observed attached to the tips of the nano-blades, indicating the successful modification with Au nanoparticles. From the EDX figures, it can be observed that the elements O, Fe, and Zn are uniformly dispersed throughout the entire sample surface, and the Au element is also relatively evenly dispersed on the sample surface.

Fig. 4 displays the cross-sectional SEM image and high-resolution TEM (HRTEM) image of the modified sample. As shown in Fig. 4a, the α-Fe_2O_3 nano-blades have lengths in the range of 500–1000 nm and exhibit a tapered structure that narrows from the base to the tip. The central region of each blade typically measures around 100–200 nm in width. In Fig. 4b, a well-defined lattice with a spacing of 0.25 nm is observed, corresponding to the (110) planes of α-Fe_2O_3, indicating high crystallinity. An amorphous ZnO layer with a thickness of approximately 4–5 nm is situated atop the α-Fe_2O_3. Such a ZnO layer thickness is considered appropriate; however, excessive thickness causes issues: holes tend to recombine before reaching the interface, and electrons face longer tunneling or bypassing paths to the conductive substrate, increasing transport resistance and significantly reducing carrier collection efficiency, thereby resulting in a decrease in PEC efficiency [30]. Au nanoparticles are found deposited on the ZnO layer. These Au nanoparticles display a lattice fringe spacing of 0.24 nm, which matches the (111) planes of metallic Au. Fig. 4c shows the lattice interface between α-Fe_2O_3 and Fe_3O_4. The lattice spacing of the Fe_3O_4 phase is approximately 0.20 nm, corresponding to the (400) plane of Fe_3O_4, which is also consistent with the XRD results. Fig. S1 presents the TEM-based elemental mapping results of the modified sample. As shown in Fig. S1a, the Au seed layer is clearly observed, and the Au nanoparticles are uniformly distributed across the surface of the α-Fe_2O_3 nano-blades. Fig. S1b further reveals that the diameter of the Au nanoparticles is ~10 nm.

3.3. Photoelectrochemical characterization

Linear sweep voltammetry (LSV) curves of the samples prepared at different annealing temperatures are shown in Fig. 5a. The solid lines represent the LSV curves of the samples under illumination, while the dashed lines represent the LSV curves under dark conditions. The sample annealed at 300 °C showed the optimal photocurrent density of 0.580 mA cm^{-2}. Considering the morphological characteristics, the uniform and dense elongated "nano-blade" structure grown on the surface shortens the carrier transport distance, resulting in superior PEC performance [31,32]. We also measured the transient photocurrent density of the samples using chronoamperometry at a constant applied bias of 0.6 V vs. Ref (equivalent to 1.6 V vs. RHE). As shown in Fig. 5b,

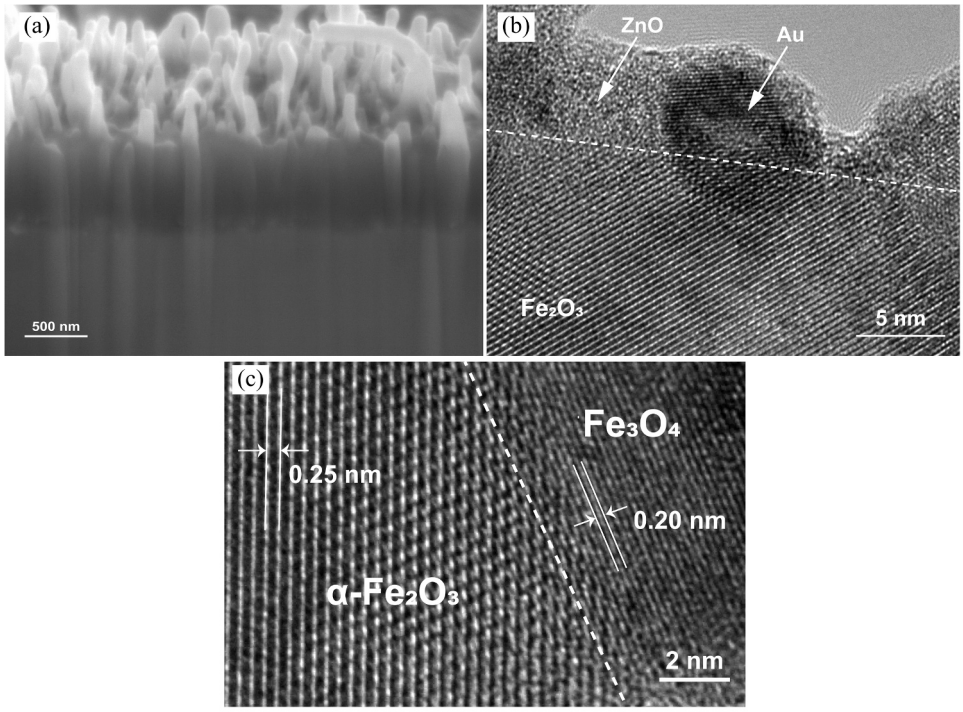

Fig. 4. (a) Cross-sectional SEM image (b,c) TEM image of α-Fe_2O_3/ZnO/Au sample.

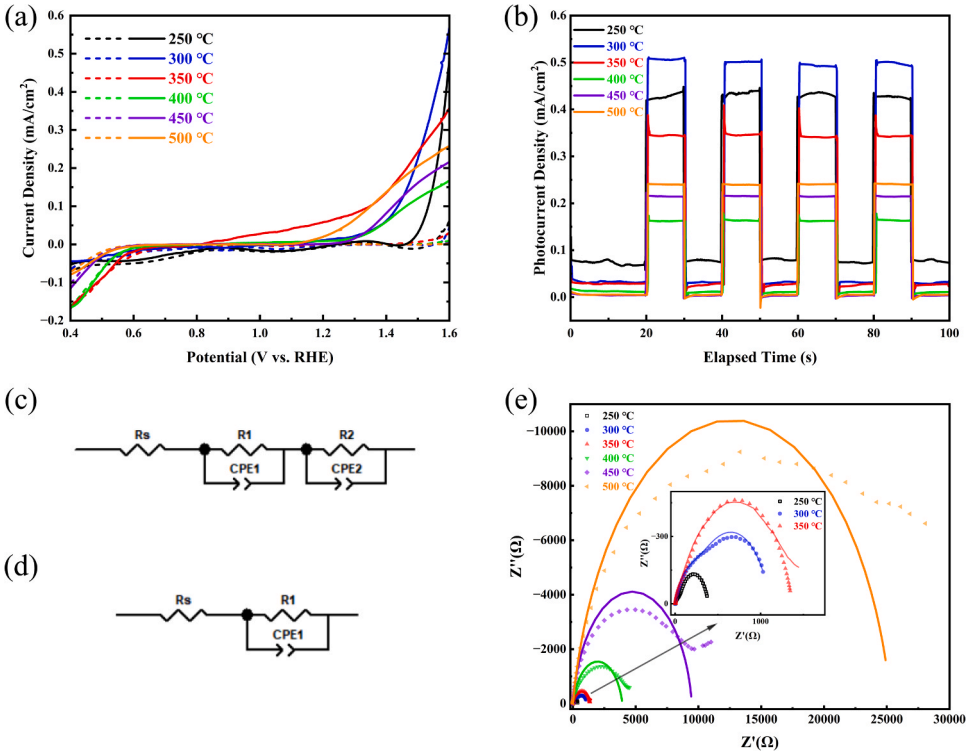

Fig. 5. (a) LSV curves (solid lines for photocurrent curves and dashed lines for current curves under dark condition); (b) chronoamperometry curves; (c & d) the equivalent circuit model; (e) Nyquist plots of the samples fabricated at different annealing temperatures.

all samples exhibited a rapid photo response.

Fig. 5e shows the Nyquist plots of the samples annealed at different temperatures. Based on the bode plots in Fig. S2a and S2b, for the samples annealed at 250 °C, 300 °C, and 350 °C, the equivalent circuit model in Fig. 5c was employed, which includes the solution resistance R_s, interface transfer resistance R_1 and interface transfer capacitance CPE_1, and another group of interface transfer resistance R_2 and interface transfer capacitance CPE_2, representing the two capacitive arcs in the Nyquist plot. These can be interpreted as the interface transfer resistance and capacitance between the Fe_3O_4 layer and Fe_2O_3 layer, and between the Fe_2O_3 layer and the electrolyte, respectively [33,34]. These results confirm the successful formation of the α-Fe_2O_3/Fe_3O_4 heterostructure,

which enhances the PEC performance by introducing an internal electric field at the interface. This built-in potential, arising from interface polarization, facilitates the separation of photogenerated electron-hole pairs-driving electrons toward the Fe_3O_4 phase and holes toward the α-Fe_2O_3 phase, thereby improving overall photocatalytic activity. Upon heterojunction formation, Fermi level alignment occurs, resulting in a downward shift of both the conduction band minimum (CBM) and valence band maximum (VBM) of Fe_3O_4 relative to those of α-Fe_2O_3, as illustrated in Fig. S3. Consequently, even if partial conversion to Fe_3O_4 occurs, the water-splitting efficiency is not compromised, as long as the redox interface between α-Fe_2O_3 and Fe_3O_4 remains intact and the thickness of the Fe_3O_4 layer is properly controlled, since the influence of the internal electric field diminishes with increasing distance [35]. For the samples annealed at 400 °C, 450 °C, and 500 °C, the equivalent circuit model in Fig. 5d was used, consisting of the solution resistance R_s, interface transfer resistance R_1 and interface transfer capacitance CPE_1, corresponding to the single capacitive arc in the Nyquist plot. As the annealing temperature increases, the samples undergo more complete oxidation with a thicker α-Fe_2O_3 layer and a thinner Fe_3O_4 layer. The influence of the Fe_3O_4 layer on PEC properties diminishes, resulting in the absence of heterostructure, combined with the overall thickening of the oxide layer, led to increased impedance, lower photocurrent density, and a decline in overall PEC performance. In summary, at an annealing temperature of 300°C, we successfully fabricated an optimal ratio of the α-Fe_2O_3/Fe_3O_4, and with uniform and dense nano-blade morphology, the PEC performance was superior compared to samples prepared at other annealing temperatures, which either failed to form heterojunction or exhibited uneven and loose or wider surface nanostructures.

We conducted PEC characterization on the samples **300°C-2h**, **300°C-2h-SC2-A1**, and **300°C-2h-SC2-A1-Au3h**. The test conditions were consistent with those mentioned above, and test results are shown in Table S2. From Fig. 6a, it can be observed that the introduction of ZnO and the modification with Au nanoparticles both effectively enhanced the photocurrent density of the photoelectrode, and all samples exhibited a rapid photo response based on Fig. 6b. The introduction of ZnO contributes to an increased photocurrent density of 0.613 mA cm^{-2} for the α-Fe_2O_3/ZnO sample **300°C-2h-SC2-A1**. In the α-Fe_2O_3 sample **300°C-2h**, illumination excites electrons from iron to oxygen atomic state, leaving holes confined to iron atoms. The iron sites with holes on the (100) plane can straightforwardly anticipate in the water oxidation reaction [36]. Upon the incorporation of ZnO, PEC improvement can be attributed to favorable band alignment at the α-Fe_2O_3/ZnO interface, where electron donation from ZnO to α-Fe_2O_3 induces a negative shift of the conduction band edge, facilitating more efficient charge separation and transfer [37]. The decoration with Au nanoparticles further improved the photocurrent density of the α-Fe_2O_3/ZnO/Au sample **300°C-2h-SC2-A1-Au3h** to 1.006 mA cm^{-2} (1.6 V vs. RHE), which is a 73.4 % increase compared to pristine α-Fe_2O_3 sample **300°C-2h**. The underlying mechanisms contributing to the enhanced PEC performance of sample **300°C-2h-SC2-A1-Au3h** will be elaborated upon in subsequent sections.

From the Nyquist plots of the samples before and after the two-step modification (shown in Fig. 6c, the equivalent circuit model in Fig. 6c was employed), after the introduction of ZnO, sample **300°C-2h-SC2-A1** exhibited a larger interface transfer resistance and a smaller interface transfer capacitance compared to the pristine sample **300°C-2h**. After the modification with Au nanoparticles, the interface transfer resistance of the sample **300°C-2h-SC2-A1-Au3h** significantly decreased, while the interface transfer capacitance markedly increased, indicating a substantial enhancement in the carrier transfer rate.

The Mott-Schottky results are shown in Fig. 6d, where all curves exhibit a positive slope, demonstrating that all samples still exhibit n-type semiconductor behavior. After the spin-coating and annealing treatment, the carrier concentration of the photoanode decreased. The

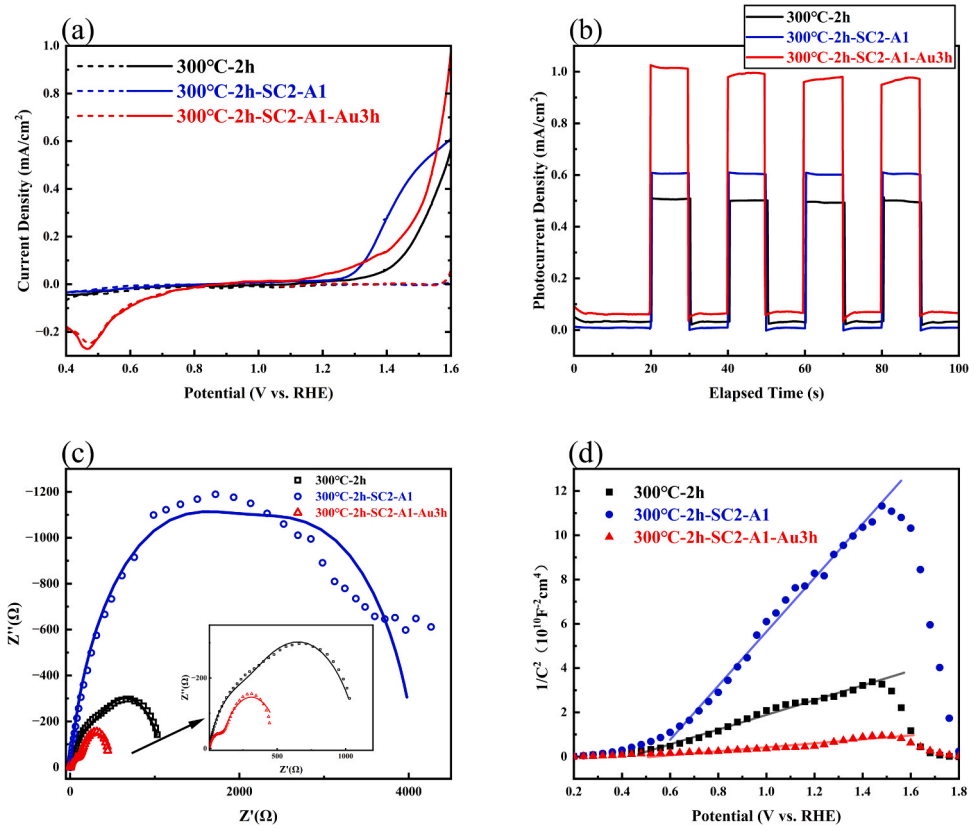

Fig. 6. (a) LSV curves (solid lines for photocurrent curves and dashed lines for current curves under dark condition) (b) chronoamperometry curves (c) Nyquist plots (d) Mott-Schottky plots of samples before and after spin coating-annealing and $HAuCl_4$ treatment.

carrier concentration of the photoanodes can be determined from the slope of the linearly fitted line via the Mott-Schottky equation Eq. (S1) and (S2). After the following modification with Au nanoparticles, the carrier concentration was then significantly increased.

3.4. Spectroscopic characterization

To investigate the light absorption characteristics of the samples, UV–vis diffuse reflectance spectroscopy (UV–vis DRS) was performed. According to Fig. 7a, the incorporation of ZnO improved the light-harvesting ability of the sample. However, the introduction of Au nanoparticles resulted in a decline in light absorption, which is likely due to partial structural damage induced during the chloroauric acid treatment process. The UV–vis DRS of Sample **300°C-2h-SC2-A1-Au3h** exhibits a noticeable peak at ~481 nm, which corresponds to the localized surface plasmon resonance (LSPR) absorption induced by the Au nanoparticle modification.

Localized surface plasmon resonance denotes the phenomenon where electrons in metal nanoparticles act as resonators triggered by an oscillating electric field. When an external electric field, such as the photoinduced electric field under illumination, is applied, the electron density is reduced on one side of the nanoparticle and elevated on the opposite side. This charge redistribution generates an internal and external electric field around the metal nanoparticle, oriented in the opposite direction to the photoinduced field. As the electron density shifts, a Coulombic restoring force is generated, causing the nanoparticles to undergo a series of oscillations, like how a spring begins to oscillate once stretched [38]. LSPR effect can strengthen the photoinduced electric field and promote electron excitation at the semiconductor interface, thereby increasing the generation rate of photogenerated electron-hole pairs [39]. This mechanism may account for the substantial increase in carrier concentration observed after Au nanoparticle modification. Under LSPR excitation, Au nanoparticles can also inject “hot electrons”, which are high-energy electrons capable of overcoming the Schottky barrier and transferring into the conduction band to actively participate in water oxidation reaction [40]. This facilitates the charge transfer process and ultimately enhances the photoelectrochemical performance.

In summary, the results of UV–vis DRS and Mott-Schottky measurements indicate that the incorporation of Au nanoparticles activates the LSPR effect, thereby enhancing the PEC performance of the sample.

To characterize the hole-electron separation efficiency of the samples, we performed PL (photoluminescence) spectroscopy on the samples before and after the two-step modification. The peak intensity in the spectrum reflects the extent of electron-hole recombination, namely, stronger peaks indicate that more electrons travel back to the valence band and recombine with holes, releasing more photon energy [41]. A 410 nm wavelength light was employed as excitation to perform steady-state PL spectroscopy on the samples before and after modification. The test results shown in Fig. 8a, where all samples exhibit a PL peak signal around 650 nm. This fluorescence response is owing to the surface micro-nanostructures. After the introduction of ZnO, the fluorescence intensity of the sample significantly decreased. Following the modification with Au nanoparticles, the fluorescence intensity further decreased. This confirms that both modification steps enhanced the hole-electron separation efficiency of the original iron oxide photoelectrode, thereby improving the PEC performance of the samples.

Moreover, we also performed time-resolved fluorescence (TRF) spectroscopy on the samples before and after modification. We used a wavelength of 375 nm as the excitation light, with the test results and fitted curves shown in Fig. 8b. We used a bi-exponential decay model to fit the curve (as shown in Eq. (S3) and (S4)). Through this method, we calculated the average fluorescence lifetimes as follows: 11.267 ns for sample **300°C-2h**, 0.273 ns for sample **300°C-2h-SC2-A1**, and 0.161 ns for sample **300°C-2h-SC2-A1-Au3h**. Consequently, the introduction of the ZnO layer decreased the fluorescence lifetime of the samples, and adornment with Au nanoparticles led to a further reduction. This suggests that the modifications formed a multilayer heterostructure within the samples, where the built-in electric field enhanced electron-hole pair separation, inhibited carrier recombination, and accelerated interfacial electron transfer, ultimately reducing the carrier fluorescence lifetime [42].

To obtain detailed surface structural information of the material and to determine the composition and valence state of the samples before and after modification, we used XPS (X-ray photoelectron spectroscopy) characterization, results are presented in Fig. 9. Fig. 9a presents the overall XPS spectra of the samples pre- and post- modification, and Fig. 9b presents the Fe 2p spectra. For sample **300°C-2h**, the Fe $2p_{3/2}$ binding energy is 710.67 eV, and the Fe $2p_{1/2}$ binding energy is 723.89 eV. The presence of satellite peaks between the Fe $2p_{3/2}$ and Fe $2p_{1/2}$ peaks confirms that the primary component of the sample surface is α-Fe_2O_3 [43,44]. After the introduction of ZnO and the modification with Au nanoparticles, the Fe $2p_{3/2}$ and Fe $2p_{1/2}$ peaks of the samples showed a shift compared to the original sample. For sample **300°C-2h-SC2-A1**, the Fe $2p_{3/2}$ binding energy is 710.07 eV, and the Fe $2p_{1/2}$ binding energy is 724.29 eV; for sample **300°C-2h-SC2-A1-Au3h**, the Fe $2p_{3/2}$ binding energy is 710.21 eV, and the Fe $2p_{1/2}$ binding energy is 724.46 eV. Each modification step led to a shift in the Fe $2p_{3/2}$ and Fe $2p_{1/2}$ peaks towards higher energy. This shift can be attributed to the oxygen vacancies on the sample surface after the modification treatments, leading to the formation of new Fe^{2+} oxidation states [45,46].

Oxygen vacancies can be further examined through the O 1s XPS spectra. The main peak of O 1s arises from the binding interaction

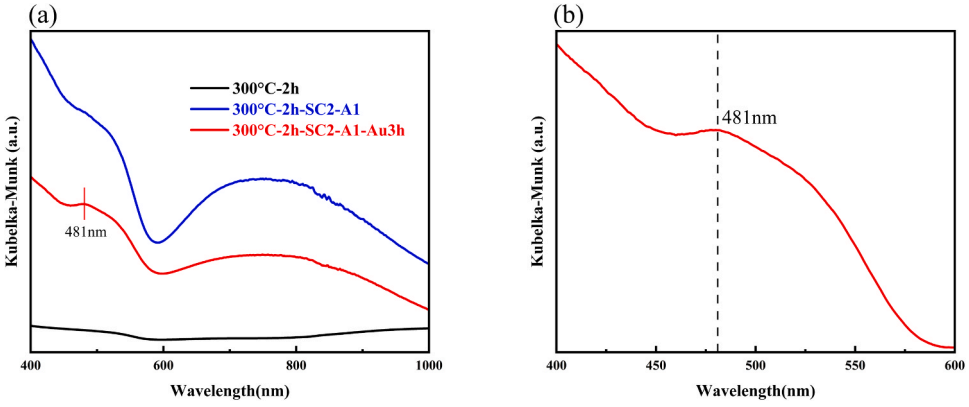

Fig. 7. UV–vis diffuse reflectance spectra of (a) samples prepared before and after spin coating-annealing and $HAuCl_4$ treatment. (b) the two-step modified sample near the absorption peak.

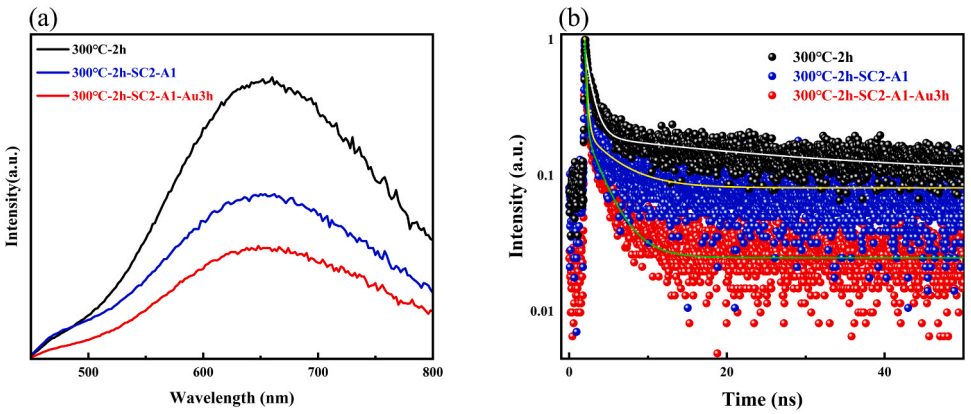

Fig. 8. (a) Photoluminescence spectra (b) photoluminescence decay curves of samples prepared before and after spin coating-annealing and $HAuCl_4$ treatment.

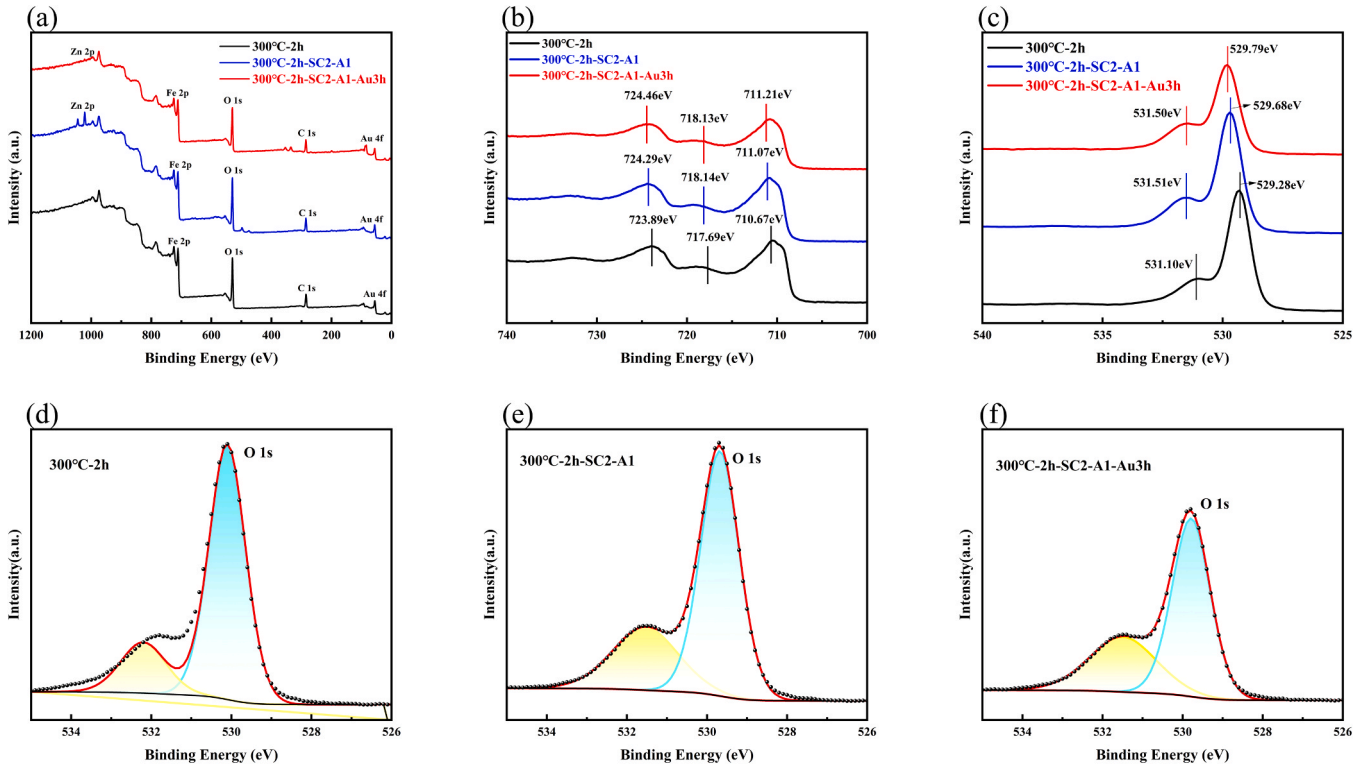

Fig. 9. XPS spectra of samples prepared before and after spin coating-annealing and $HAuCl_4$ treatment. (a) Overall XPS spectra; (b) Fe 2p XPS spectra; (c) O 1s XPS spectra; and O 1s peak fitting plots of (d) sample **300°C-2h**, (e) sample **300°C-2h-SC2-A1**, (f) sample **300°C-2h-SC2-A1-Au3h**.

between oxygen atoms and the corresponding metal atoms [47,48], while the satellite peak of O 1s is associated with oxygen vacancies [49]. We performed peak deconvolution analysis on the O 1s XPS spectra of the samples before and after modification, as shown in Fig. 9d–f. For the samples **300°C-2h**, **300°C-2h-SC2-A1**, and **300°C-2h-SC2-A1-Au3h**, the intensity ratios of the satellite peak near 531 eV to the main peak at 529 eV are 0.20, 0.26, and 0.31, respectively. This indicates that the introduction of ZnO on the sample surface and subsequent modification with Au nanoparticles increased the concentration of oxygen vacancies compared to the samples before each modification step. The concentration of oxygen vacancies acts as a critical factor in the oxygen evolution reaction (OER) [48,50], ultimately leading to enhanced PEC efficiency with each modification.

4. Conclusion

In summary, we prepared α-Fe_2O_3 photoanodes by directly oxidizing and annealing high-purity iron foil in air, managed to develop a uniform slender nano-blade structure and an α-Fe_2O_3/Fe_3O_4 heterojunction on Fe substrate, with a photocurrent density of 0.580 mA cm^{-2} (1.6 V vs. RHE). Additionally, we successfully developed an enhanced α-Fe_2O_3/ZnO/Au photoelectrode system. The integration of ZnO layer and Au nanoparticles led to notable improvements in PEC performance, demonstrated by a photocurrent density of 1.006 mA cm^{-2} (1.6 V vs. RHE), showing a 73.4 % increase compared to pristine hematite. The enhancement is the result of the combined yet distinct contributions of each modification component. The α-Fe_2O_3/Fe_3O_4 heterojunction introduces an internal electric field that promotes charge separation and suppresses recombination. The ultrathin ZnO layer facilitates favorable band alignment and provides an additional charge transport pathway at

the semiconductor-electrolyte interface. Meanwhile, the plasmonic Au nanoparticles enhance visible-light absorption via LSPR and contribute hot electrons that participate in interfacial redox reactions. These individual effects work synergistically to significantly improve charge separation and PEC performance, highlighting the effectiveness of the integrated multi-step modification strategy.

CRediT authorship contribution statement

Hao Yuan: Writing – review & editing, Validation, Data curation. **Ying Yang:** Writing – review & editing, Validation, Investigation, Data curation. **Jiaheng Gao:** Writing – review & editing, Writing – original draft, Resources, Methodology, Investigation, Formal analysis, Data curation, Conceptualization. **Maojun Zheng:** Supervision, Project administration, Funding acquisition, Conceptualization. **Wenzhong Shen:** Supervision, Project administration. **Hao Chen:** Writing – review & editing, Validation. **Yunlong Fan:** Writing – review & editing, Validation.

Declaration of Competing Interest

The authors declare the following financial interests/personal relationships which may be considered as potential competing interests: Maojun Zheng reports financial support was provided by Science and Technology Commission of Shanghai Municipality. Maojun Zheng reports financial support was provided by National Natural Science Foundation of China. If there are other authors, they declare that they have no known competing financial interests or personal relationships that could have appeared to influence the work reported in this paper.

Acknowledgments

This research was supported by the Science and Technology Commission of Shanghai Municipality (Grant No. 21ZR1434900) and National Natural Science Foundation of China (Grant No. 11574203).

Appendix A. Supporting information

Supplementary data associated with this article can be found in the online version at doi:10.1016/j.jallcom.2025.182416.

References

[1] World Energy Outlook 2023. ⟨https://www.iea.org/reports/world-energy-outlook-2023⟩.
[2] A. Fujishima, K. Honda, Electrochemical photolysis of water at a semiconductor electrode, Nature 238 (5358) (1972) 37–38, https://doi.org/10.1038/238037a0.
[3] M. Pavlenko, K. Siuzdak, E. Coy, et al., Enhanced solar-driven water splitting of 1D core-shell Si/TiO_2/ZnO nanopillars, Int. J. Hydrogen Energy 45 (50) (2020) 26426–26433, https://doi.org/10.1016/j.ijhydene.2019.11.231.
[4] S.M. Fawzy, M. Omar, N.K. Allam, Photoelectrochemical water splitting by defects in nanostructured multinary transition metal oxides, Sol. Energy Mater. Sol. Cells 194 (2019) 184–194, https://doi.org/10.1016/j.solmat.2019.02.011.
[5] R. Elakkiya, R. Ramkumar, G. Maduraiveeran, Flower-like nickel-cobalt oxide nanomaterials as bi-functional catalyst for electrochemical water splitting, Mater. Res. Bull. 116 (2019) 98–105, https://doi.org/10.1016/j.materresbull.2019.04.016.
[6] Y. Guo, X. Zhou, J. Tang, et al., Multiscale structural optimization: highly efficient hollow iron-doped metal sulfide heterostructures as bifunctional electrocatalysts for water splitting, Nano Energy 75 (2020) 104913, https://doi.org/10.1016/j.nanoen.2020.104913.
[7] Q. Zhang, W. Chen, G. Chen, et al., Bi-metallic nitroxide nanodot-decorated tri-metallic sulphide nanosheets by on-electrode plasma-hydrothermal sprouting for overall water splitting, Appl. Catal. B Environ. 261 (2020) 118254, https://doi.org/10.1016/j.apcatb.2019.118254.
[8] M. Batouche, T. Seddik, T.V. Vu, et al., Ternary sulfides $BaLa_2S_4$ and $CaLa_2S_4$ as promising photocatalytic water splitting and thermoelectric materials: first-principles DFT calculations, Int. J. Hydrogen Energy 45 (43) (2020) 22600–22612, https://doi.org/10.1016/j.ijhydene.2019.06.124.
[9] D. Wei, Y. Ding, Z. Li, Noble-metal-free Z-Scheme MoS_2-CdS/WO_3-MnO_2 nanocomposites for photocatalytic overall water splitting under visible light, Int. J. Hydrogen Energy 45 (35) (2020) 17320–17328, https://doi.org/10.1016/j.ijhydene.2020.04.160.
[10] Q. Cai, Z. Liu, C. Han, et al., $CuInS_2$/Sb_2S_3 heterostructure modified with noble metal co-catalyst for efficient photoelectrochemical water splitting, J. Alloy. Compd. 795 (2019) 319–326, https://doi.org/10.1016/j.jallcom.2019.04.312.
[11] S. Hu, X. Sun, Y. Zhao, et al., The effective photocatalytic water splitting to simultaneously produce H_2 and H_2O_2 over Pt loaded K-g-C_3N_4 catalyst, J. Taiwan Inst. Chem. Eng. 107 (2020) 129–138, https://doi.org/10.1016/j.jtice.2019.12.007.
[12] G. Liu, M. Xue, Q. Liu, et al., Facile synthesis of C-doped hollow spherical g-C_3N_4 from supramolecular self-assembly for enhanced photoredox water splitting, Int. J. Hydrogen Energy 44 (47) (2019) 25671–25679, https://doi.org/10.1016/j.ijhydene.2019.08.056.
[13] A.S. Reddy, J. Kim, An efficient g-C_3N_4-decorated CdS-nanoparticle-doped Fe_3O_4 hybrid catalyst for an enhanced H_2 evolution through photoelectrochemical water splitting, Appl. Surf. Sci. 513 (2020) 145836, https://doi.org/10.1016/j.apsusc.2020.145836.
[14] K. Sivula, F. Le Formal, M. Grätzel, Solar water splitting: progress using hematite (α-Fe_2O_3) photoelectrodes, ChemSusChem 4 (4) (2011) 432–449, https://doi.org/10.1002/cssc.201000416.
[15] H. Liu, X. Fan, Y. Li, et al., Hematite-based photoanodes for photoelectrochemical water splitting: performance, understanding, and possibilities, J. Environ. Chem. Eng. 11 (1) (2023) 109224, https://doi.org/10.1016/j.jece.2022.109224.
[16] K.M. Rosso, D.M.A. Smith, M. Dupuis, An ab initio model of electron transport in hematite (α-Fe_2O_3) basal planes, J. Chem. Phys. 118 (14) (2003) 6455–6466, https://doi.org/10.1063/1.1558534.
[17] Y. Hou, C. Zheng, Z. Zhu, et al., Microwave-assisted fabrication of porous hematite photoanodes for efficient solar water splitting, Chem. Commun. 52 (42) (2016) 6888–6891, https://doi.org/10.1039/C6CC02404A.
[18] K. Sivula, F. Le Formal, M. Grätzel, Solar water splitting: progress using hematite (α-Fe_2O_3) photoelectrodes, ChemSusChem 4 (4) (2011) 432–449, https://doi.org/10.1002/cssc.201000416.
[19] F. Mohamed, M. Rabia, M. Shaban, Synthesis and characterization of biogenic iron oxides of different nanomorphologies from pomegranate peels for efficient solar hydrogen production, J. Mater. Res. Technol. 9 (3) (2020) 4255–4271, https://doi.org/10.1016/j.jmrt.2020.02.052.
[20] H.J. Ahn, M.J. Kwak, J.S. Lee, et al., Nanoporous hematite structures to overcome short diffusion lengths in water splitting, J. Mater. Chem. A 2 (47) (2014) 19999–20003, https://doi.org/10.1039/C4TA04890C.
[21] L.K. Dhandole, T.S. Koh, P. Anushkkaran, et al., Enhanced charge transfer with tuning surface state in hematite photoanode integrated by niobium and zirconium co-doping for efficient photoelectrochemical water splitting, Appl. Catal. B Environ. 315 (2022) 121538, https://doi.org/10.1016/j.apcatb.2022.121538.
[22] M.G. Ahmed, M. Zhang, Y.F. Tay, et al., Surface modification of hematite photoanodes with CeO_x cocatalyst for improved photoelectrochemical water oxidation kinetics, ChemSusChem 13 (20) (2020) 5489–5496, https://doi.org/10.1002/cssc.202001135.
[23] S. Seenivasan, S. Adhikari, D.H. Kim, Surface restructuring of hematite photoanodes through ultrathin $NiFeO_x$ catalyst: amplified charge collection for solar water splitting and pollutant degradation, Chem. Eng. J. 422 (2021) 130137, https://doi.org/10.1016/j.cej.2021.130137.
[24] A. Subramanian, M.A. Mahadik, J.W. Park, et al., An effective strategy to promote hematite photoanode at low voltage bias via Zr^{4+}/Al^{3+} codoping and CoO_x OER co-catalyst, Electrochim. Acta 319 (2019) 444–455, https://doi.org/10.1016/j.electacta.2019.06.149.
[25] M.J. Kang, Y.S. Kang, Ultrathin insulating under-layer with a hematite thin film for enhanced photoelectrochemical (PEC) water splitting activity, J. Mater. Chem. A 3 (30) (2015) 15723–15728, https://doi.org/10.1039/C5TA03468J.
[26] L. Wang, H. Hu, N.T. Nguyen, et al., Plasmon-induced hole-depletion layer on hematite nanoflake photoanodes for highly efficient solar water splitting, Nano Energy 35 (2017) 171–178, https://doi.org/10.1016/j.nanoen.2017.03.035.
[27] D.L.A. De Faria, S. Venâncio Silva, M.T. de Oliveira, Raman microspectroscopy of some iron oxides and oxyhydroxides, J. Raman Spectrosc. 28 (11) (1997) 873–878, https://doi.org/10.1002/(SICI)1097-4555(199711)28:11%3C873::AID-JRS177%3E3.0.CO;2-B.
[28] L. Yuan, R. Cai, J.I. Jang, et al., Morphological transformation of hematite nanostructures during oxidation of iron, Nanoscale 5 (16) (2013) 7581–7588, https://doi.org/10.1039/C3NR01669B.
[29] L. Xi, P.S. Bassi, S.Y. Chiam, et al., Surface treatment of hematite photoanodes with zinc acetate for water oxidation, Nanoscale 4 (15) (2012) 4430–4433, https://doi.org/10.1039/C2NR30862B.
[30] S. Chen, J. Li, J. Bai, et al., Electron blocking and hole extraction by a dual-function layer for hematite with enhanced photoelectrocatalytic performance, Appl. Catal. B Environ. 237 (2018) 175–184, https://doi.org/10.1016/j.apcatb.2018.05.068.
[31] A. Chnani, S. Strehle, Hematite nanowire and nanoflake-decorated photoelectrodes: implications for photoelectrochemical water splitting, ACS Appl. Nano Mater. 5 (1) (2021) 1016–1022, https://doi.org/10.1021/acsanm.1c03684.
[32] R. Zhang, Y. Fang, T. Chen, et al., Enhanced photoelectrochemical water oxidation performance of Fe_2O_3 nanorods array by S doping, ACS Sustain. Chem. Eng. 5 (9) (2017) 7502–7506, https://doi.org/10.1021/acssuschemeng.7b01799.
[33] W. Yang, T. Moehl, E. Service, et al., Operando analysis of semiconductor junctions in multi-layered photocathodes for solar water splitting by impedance spectroscopy, Adv. Energy Mater. 11 (9) (2021) 2003569, https://doi.org/10.1002/aenm.202003569.
[34] T. Moehl, W. Cui, R. Wick-Joliat, et al., Resistance-based analysis of limiting interfaces in multilayer water splitting photocathodes by impedance spectroscopy, Sustain. Energy Fuels 3 (8) (2019) 2067–2075, https://doi.org/10.1039/C9SE00248K.

[35] J. Leduc, Y. Goenuellue, P. Ghamgosar, et al., Electronically-coupled phase boundaries in α-Fe_2O_3/Fe_3O_4 nanocomposite photoanodes for enhanced water oxidation, ACS Appl. Nano Mater. 2 (1) (2019) 334–342, https://doi.org/10.1021/acsanm.8b01936.
[36] S. Shen, S.A. Lindley, X. Chen, et al., Hematite heterostructures for photoelectrochemical water splitting: rational materials design and charge carrier dynamics, Energy Environ. Sci. 9 (9) (2016) 2744–2775, https://doi.org/10.1039/C6EE01845A.
[37] S. Chen, J. Li, J. Bai, et al., Electron blocking and hole extraction by a dual-function layer for hematite with enhanced photoelectrocatalytic performance, Appl. Catal. B Environ. 237 (2018) 175–184, https://doi.org/10.1016/j.apcatb.2018.05.068.
[38] S.C. Warren, E. Thimsen, Plasmonic solar water splitting, Energy Environ. Sci. 5 (1) (2012) 5133–5146, https://doi.org/10.1039/C1EE02875H.
[39] J. Lee, T. Javed, T. Skeini, et al., Bioconjugated Ag nanoparticles and CdTe nanowires: metamaterials with field-enhanced light absorption, Angew. Chem. 118 (29) (2006) 4937–4941, https://doi.org/10.1002/anie.200600356.
[40] Y. Liu, Z. Xu, M. Yin, et al., Enhanced photoelectrocatalytic performance of α-Fe_2O_3 thin films by surface plasmon resonance of Au nanoparticles coupled with surface passivation by atom layer deposition of Al_2O_3, Nanoscale Res. Lett. 10 (2015) 1–8, https://doi.org/10.1186/s11671-015-1077-y.
[41] L.R. Nagappagari, J. Lee, H. Lee, et al., Energy and environmental applications of Sn^{4+}/Ti^{4+} doped α-Fe_2O_3@Cu_2O/CuO photoanode under optimized photoelectrochemical conditions, Environ. Pollut. 271 (2021) 116318, https://doi.org/10.1016/j.envpol.2020.116318.
[42] Gao C., Yu H., Zhang L., et al. Ultrasensitive paper-based photoelectrochemical sensing platform enabled by the polar charge carriers-created electric field. https://doi.org/10.1021/acs.analchem.9b05611.
[43] J.D. Desai, H.M. Pathan, S.K. Min, et al., FT-IR, XPS and PEC characterization of spray deposited hematite thin films, Appl. Surf. Sci. 252 (5) (2005) 1870–1875, https://doi.org/10.1016/j.apsusc.2005.03.135.
[44] Y.S. Hu, A. Kleiman-Shwarsctein, A.J. Forman, et al., Pt-doped α-Fe_2O_3 thin films active for photoelectrochemical water splitting, Chem. Mater. 20 (12) (2008) 3803–3805, https://doi.org/10.1021/cm800144q.
[45] J. Lu, X. Jiao, D. Chen, et al., Solvothermal synthesis and characterization of Fe_3O_4 and γ-Fe_2O_3 nanoplates, J. Phys. Chem. C 113 (10) (2009) 4012–4017, https://doi.org/10.1021/jp810583e.
[46] X. Teng, D. Black, N.J. Watkins, et al., Platinum-maghemite core-shell nanoparticles using a sequential synthesis, Nano Lett. 3 (2) (2003) 261–264, https://doi.org/10.1021/nl025918y.
[47] X.F. Lu, D.J. Wu, R.Z. Li, et al., Hierarchical $NiCo_2O4$ nanosheets@hollow microrod arrays for high-performance asymmetric supercapacitors, J. Mater. Chem. A 2 (13) (2014) 4706–4713, https://doi.org/10.1039/C3TA14930G.
[48] F. Lei, Y. Sun, K. Liu, et al., Oxygen vacancies confined in ultrathin indium oxide porous sheets for promoted visible-light water splitting, J. Am. Chem. Soc. 136 (19) (2014) 6826–6829, https://doi.org/10.1021/ja501866r.
[49] J. Bao, X. Zhang, B. Fan, et al., Ultrathin spinel-structured nanosheets rich in oxygen deficiencies for enhanced electrocatalytic water oxidation, Angew. Chem. 127 (25) (2015) 7507–7512, https://doi.org/10.1002/ange.201502226.
[50] J. Moir, N. Soheilnia, K. Liao, et al., Activation of ultrathin films of hematite for photoelectrochemical water splitting via H_2 treatment, ChemSusChem 8 (9) (2015) 1557–1567, https://doi.org/10.1002/cssc.201402945.